MONTANA STATE UNIVERSITY LIBRARY

Raman vibrations, domain structures, and photovoltaic effects in A-site La-modified BiFeO 3 multiferroic ceramics

Authors: C.- S. Tu, C.- S. Chen, P.- Y. Chen, Z.- R. Xu, Yves U. Idzerda, V. Hugo Schmidt, M.- Q. Lyu, T.- S. Chan, and C. Y. Liu

This is the peer reviewed version of the following article: see full citation below, which has been published in final form at https://doi.org/10.1111/jace.13983. This article may be used for non-commercial purposes in accordance with Wiley Terms and Conditions for Self-Archiving.

C.-S. Tu, C.-S. Chen, P.-Y. Chen, Z.-R. Xu, Y.U. Idzerda, V.H. Schmidt, M.-Q. Lyu, T.-S. Chan, and C.Y. Liu, “Raman vibrations, domain structures, and photovoltaic effects in A-site La-modified BiFeO 3 multiferroic ceramics,” to appear in Journal of the American Ceramic Society (2015). doi: 10.1111/jace.13983.

Made available through Montana State University’s ScholarWorks
scholarworks.montana.edu

Raman Vibrations, Domain Structures, and Photovoltaic Effects in A-Site La-Modified $BiFeO_3$ Multiferroic Ceramics

Chi-Shun Tu,[‡,†] Cheng-Sao Chen,[§] Pin-Yi Chen,[¶] Zhe-Rui Xu,[‡] Yves U. Idzerda,[‖] V. Hugo Schmidt,[‖] Ming-Quan Lyu,[¶] Ting-Shan Chan,[††] and Chun-Yen Lin[‡]

[‡]Department of Physics, Fu Jen Catholic University, New Taipei City 24205, Taiwan

[§]Department of Mechanical Engineering, Hwa Hsia University of Technology, New Taipei City 23567, Taiwan

[¶]Department of Mechanical Engineering, Ming Chi University of Technology, New Taipei City 24301, Taiwan

[‖]Department of Physics, Montana State University, Bozeman, Montana 59717

[††]National Synchrotron Radiation Research Center, Hsinchu 30076, Taiwan

Micro-Raman spectroscopy, X-ray diffraction, high-resolution transmission electron microscopy (TEM), oxygen vacancies, synchrotron X-ray absorption spectroscopy, magnetizations, optical band gaps, and photovoltaic (PV) effects have been studied in $(Bi_{1-x}La_x)FeO_3$ (BFO100*x*L) ceramics for $x = 0.0$, 0.05, 0.10, and 0.15. XRD, Raman spectra, and TEM confirm a rhombohedral *R*3*c* symmetry with the tilted FeO_6 oxygen octahedra in all compounds. The low-frequency Raman vibrations become broader and shift toward higher frequency as La^{3+} increases. Fe K-edge synchrotron X-ray absorptions reveal that Fe^{3+} valence and Fe–O–Fe bond angle are not modified by the La^{3+} substitution. All compounds exhibit a linear antiferromagnetic feature. Optical transmission reveals band gaps in the range of 2.22–2.24 eV. The heterostructures of indium tin oxide (ITO) film/$(Bi_{1-x}La_x)FeO_3$ ceramics/Au film show a *p–n* junction-like *I–V* characteristic behavior. The maximal PV power conversion efficiency can reach 0.19% in ITO/BFO15L/Au under illumination of $\lambda = 405$ nm. A junction-like theoretical model can reasonably describe open-circuit voltage and short-circuit current as a function of illumination intensity.

I. Introduction

BISMUTH ferrite $BiFeO_3$ (BFO) materials have been widely studied because of their room-temperature antiferromagnetic (T_N~630 K) and ferroelectric ordering (T_C ~1100 K).[1] BFO has a rhombohedral perovskite *R*3c structure, in which the cations (Bi^{3+} and Fe^{3+}) displace along the $[111]_C$ direction with FeO_6 octahedra rotated antiphase around the rhombohedral axis.[2] A-site Bi^{3+} has a stereochemically active $6s^2$ lone pair, which activates a hybridization of Bi 6*p* and O 2*p* states, and causes an off-centering displacement of Bi^{3+} toward O^{2-} to induce ferroelectricity.[3] The magnetic moment of Fe^{3+} ions of BFO are in a G-type AFM ordering such that each spin is surrounded by six antiparallel neighbor spins.[1,4] The dynamics of domain walls in polycrystalline BFO plays an important bridging role between local conductivity and macroscopic electromechanical properties.[5]

Electric leakage, low remanent polarization, and weak magnetoelectric coupling have limited BFO for applications.[1] To reduce the current leakage and suppression of the magnetic spin cycloid, many studies have focused on the substitution of rare-earth elements onto the A-site Bi^{3+} ions of the perovskite cell.[6] La doping in BFO ceramics can improve magnetic response, and reduce the leakage current and dielectric loss.[6,7] Rhombohedral *R*3*c* symmetry of $(Bi_{1-x}La_x)FeO_3$ has been reported in different La concentration ranges, for examples, $x \le 0.125$,[6,8] $x \le 0.15$,[8–11] $x \le 0.20$,[12] $x \le 0.25$,[13] and $x \le 0.30$.[14,15] From synchrotron XRD and high-resolution TEM, an incommensurately modulated phase has been observed for $0.19 \le x \le 0.30$.[7,11] An orthorhombic *Pnma* symmetry was proposed for $x \ge 0.50$.[11] First-principles calculations using density functional theory (DFT) in $(Bi_{1-x}La_x)FeO_3$ have shown that the most stable phases are rhombohedral *R*3*c* for $x = 0.1$ and orthorhombic *Pnma* for $x = 0.2$ and 0.3.[16] According to the Kohn–Sham energy,[9,17] the phase boundary between *R*3*c* and *Pnma* symmetries was predicted near $x = 0.30$. Two degenerate orthorhombic *Pnma* and $Pna2_1$ structures are theoretically stable in the region of $0.3 \le x \le 0.65$.[6,18]

Weak ferromagnetic magnetization has been observed in A-site rare-earth-doped $(Bi_{1-x}A_x)FeO_3$ (A = La, Nd, Sm, Er) ceramics.[19–26] Unsaturated ferroelectric hysteresis loops have been observed in $(Bi_{1-x}La_x)FeO_3$ ceramics.[20] The magnitudes of remanent magnetization (M_r) and coercive field (H_c) increase with La content,[22] perhaps due to the suppression of the cycloidal spin structure[23] and increased magnetoelectric coupling.[27] The weak ferromagnetism in $(Bi_{1-x}La_x)FeO_3$ ceramics can be attributed to the canting of the antiferromagnetic spins by the modification of the antiparallel sublattice magnetization of Fe^{3+}.[22] Recent work of Nd-substituted BFO ceramics has suggested that homogeneity of sample can be improved by using multiple heating cycles.[28]

$BiFeO_3$ has been considered a *p*-type semiconducting material resulting from the loss of Bi^{3+} cations during the high-temperature synthesis process, which causes vacancies to act as *p*-type centers for accepting electrons.[29] First-principles calculations suggested that Bi vacancies (V_{Bi}) have lower formation energy than oxygen vacancies under oxygen-rich condition and V_{Bi} become the electron-acceptor defects.[30] In BFO, the Fe–O bond length (~1.93 Å) is shorter than the Bi–O bond length (~2.31 Å), thus the formation of Bi vacancies is easier than formation of Fe vacancies.[31] *P*-type BFO and *n*-type ITO films have been reported, respectively, with carrier densities of n_p~10^{23} m^{-3} and n_n~10^{26}–10^{27} m^{-3}.[32,33] BFO films and crystals have shown interesting photovoltaic

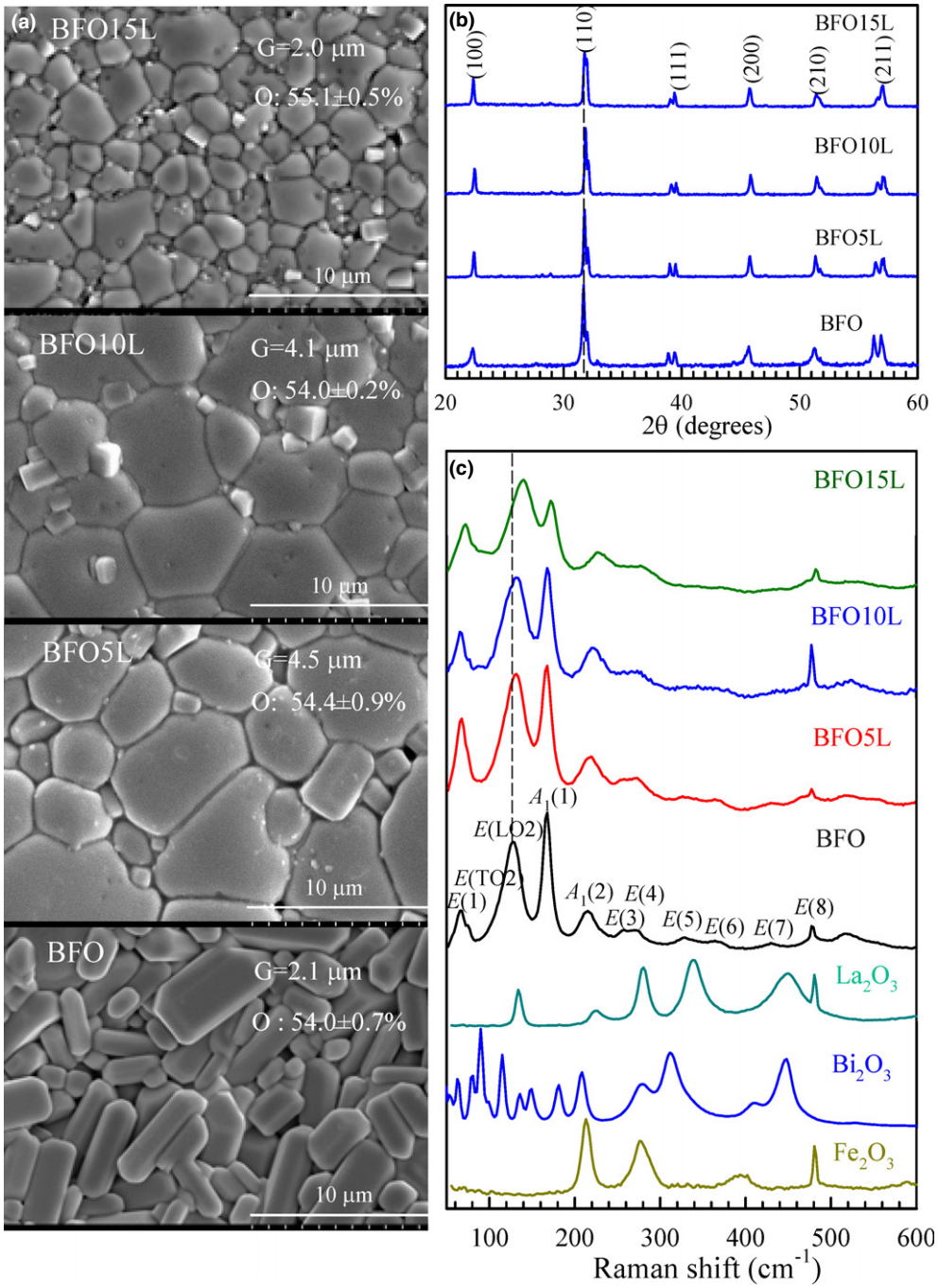


Fig. 1. (a) SEM grain morphologies, (b) XRD spectra, and (c) Raman spectra of as-sintered ceramics. "G" and "O" represent average grain sizes and oxygen atomic ratios determined by SEM EDS.

(PV) responses and photoconductivity.[34–37] PV properties of the alkaline-earth (Ca^{2+}, Sr^{2+}, Ba^{2+})-doped BFO ceramics with ITO (top) and Au (bottom) electrodes have shown dependences on thickness, light wavelength, and intensity.[38–40] The PV open-circuit voltage and short-circuit current have been described by a theoretical model, which is based on the photo-excited carriers in the interface.[38]

The Raman spectra of BFO ceramics reveal two anomalies in the vicinities of the Neel temperature (T_N ~645 K) and of 140–200 K, the temperature range of a spin-reorientation transition.[41] Direct optical band gaps of 2.55–2.75 eV have been reported for rhombohedral BFO films.[42–44] Based on optical transmission and the Tauc equation,[45] optical band gaps of $(Bi_{1-x}La_x)FeO_3$ (x = 0.0–0.30) films are in the range of 2.60–2.68 eV and decrease with increasing La concentration.[26]

Previous studies of A-site-doped BFO materials[6] have focused on structure, and on photo-induced electric and optical properties. However, the correlations among optical responses, domain structure, oxygen vacancies, vibration modes, electronic valence, magnetic response, and A-site substitution cation still lack exploration. This work is mainly to study the effects of La^{3+} doping on structural symmetry, domain structure, oxygen vacancies, Fe valence, Fe–O–Fe interatomic distance, magnetization, optical band gap, and PV effects of $(Bi_{1-x}La_x)FeO_3$ (x = 0.0–0.15) prepared under the same synthesizing conditions.

II. Experimental Procedure

$BiFeO_3$ (BFO), $(Bi_{0.95}La_{0.05})FeO_3$ (BFO5L), $(Bi_{0.90}La_{0.10})FeO_3$ (BFO10L), and $(Bi_{0.85}La_{0.15})FeO_3$ (BFO15L) ceramics

were prepared by the solid-state reaction, in which Bi_2O_3, La_2O_3, and Fe_2O_3 powders (purity ≥99.0%) were weighed, respectively, in the respective ratios of 1.1:0:1.0, 0.95:0.05:1.0, 0.90:0.10:1.0, and 0.85:0.15:1.0. The powders were mixed in an agate mortar with alcohol as a medium for more than 24 h. The dried mixtures were calcined at 800°C (3 h) for all compounds, and then sintered at 830°C (10 h) for BFO and 870°C (3 h) for BFO5L, BFO10L, and BFO15L.

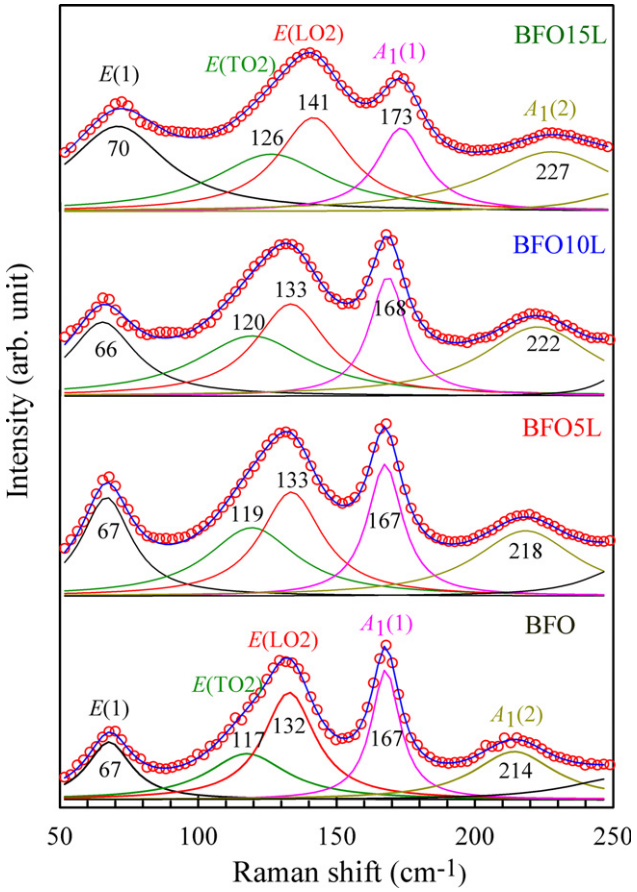


Fig. 2. Experimental Raman spectra and fitting modes in the region of 50–250 cm^{-1}.

X-ray diffraction, grain morphologies, and oxygen vacancies of the as-sintered ceramics were, respectively, measured using a Rigaku Corporation (Tokyo, Japan) Multiplex Diffractometer and a Hitachi Corporation (Tokyo, Japan) S-3400N scanning electron microscope (SEM/EDS). A high-resolution TEM (JEM-2100 LaB_6, JEOL Ltd., Tokyo, Japan) was used to study the symmetry groups and domain structures. Micro-Raman spectra were measured using a Raman instrument (XperRam 200; Nanobase Inc., Seoul, Korea) equipped with a green laser of $\lambda = 532$ nm.[40] To determine the oxidation states, the synchrotron X-ray absorption near-edge structure (XANES) and extended X-ray absorption fine structure (EXAFS) spectra of Fe K-edge were recorded in transmission mode at the 01C1 beam line of the National Synchrotron Radiation Research Center in Taiwan. The soft X-ray absorption spectra (XAS) of the Fe L_3-edge were studied in total electron yield via sample current mode at the 6.3.1.1 beam line of the Advanced Light Source Berkeley National Laboratory. For PV effects, ITO and Au films were deposited on ceramic surfaces by dc sputtering. The sample thickness and illuminated area (also area of ITO) are 0.2 mm and ~0.15 cm^2. A diode laser of $\lambda = 405$ nm was used for illumination. The optical transmission of ITO film is ~80% at $\lambda = 405$ nm. The optical transmission spectra were measured using a Cary 5E UV-Vis-NIR spectrometer (Agilent Technologies, Santa Clara, CA).

III. Results and Discussion

Grain morphologies of the as-sintered ceramics are shown in Fig. 1(a) and the average grain sizes (as represented by "*G*") are, respectively, 2.1, 4.5, 4.1, and 2.0 μm for BFO, BFO5L, BFO10L, and BFO15L. Figure 1(a) also gives average oxygen molar ratios measured from five different positions of each sample as indicated by "O". The theoreti-

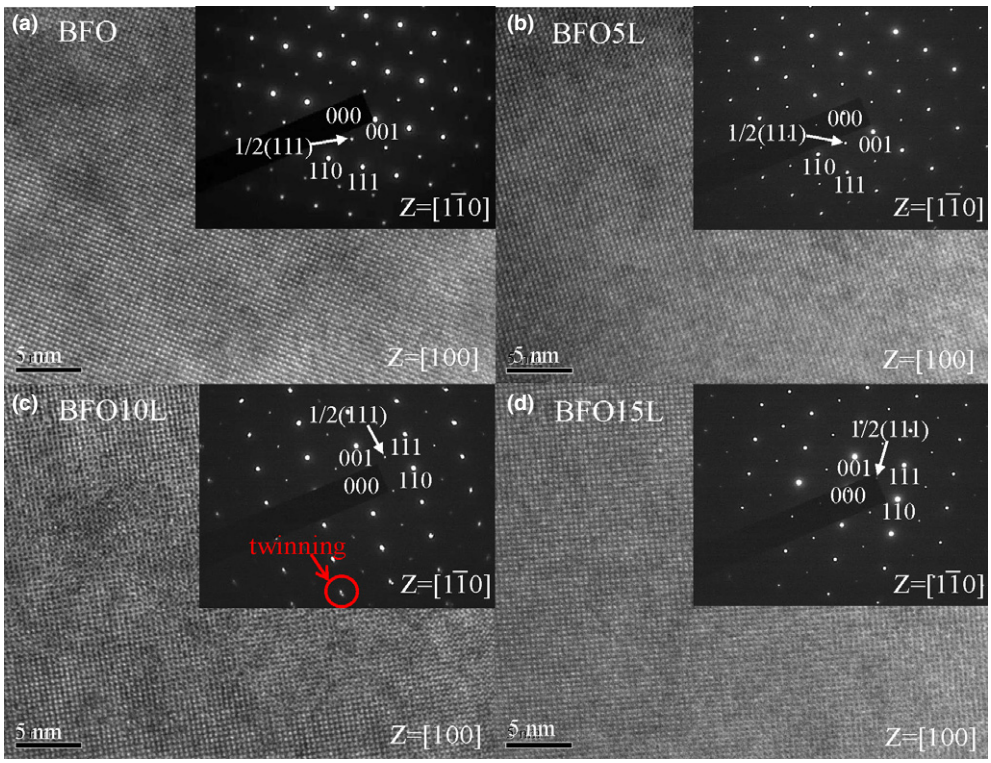


Fig. 3. Bright-field TEM images and SADPs of BFO, BFO5L, BFO10L, and BFO15L.

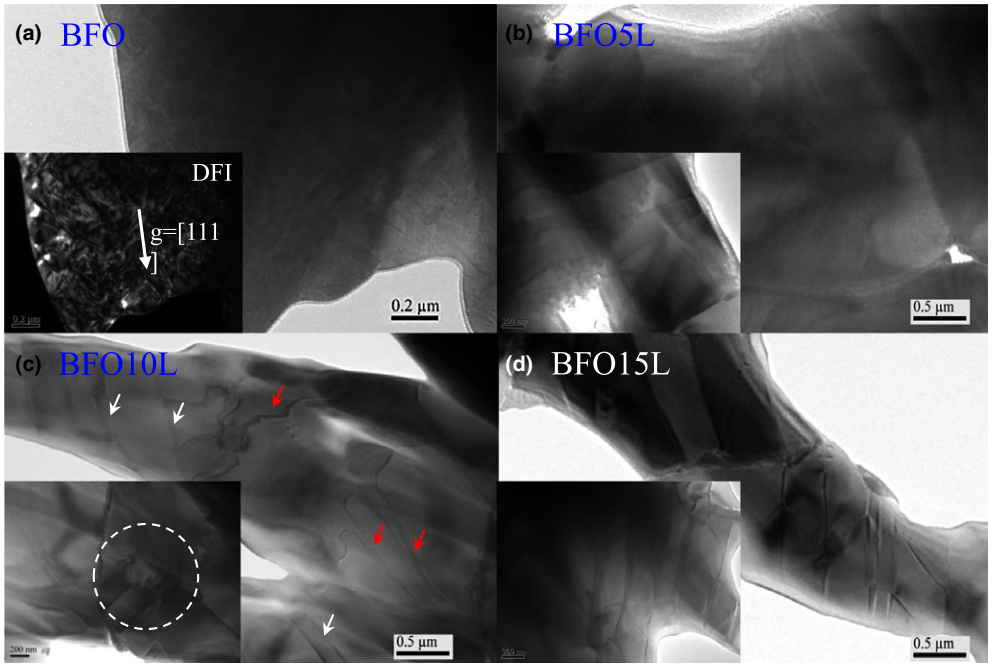


Fig. 4. Domain structures measured by high-resolution TEM. The inset is the dark-field image (DFI) viewed along the diffraction vector g = [111]. Red and white arrows in (c) indicate 180° and non-180° domain walls, respectively.

cal oxygen atomic ratio is 60% in the $BiFeO_3$ perovskite unit cell. BFO5L and BFO15L exhibit slightly less oxygen vacancies (OVs) than the pure BFO. The average oxygen molar ratio of BFO10L is similar to the pure BFO. The results suggest that La^{3+} doping can reduce the formation of oxygen vacancies. This is consistent with the suggestion that the doping stabilizes $BiFeO_3$ for the formation of defects.[6] X-ray diffraction (XRD) spectra of as-sintered samples at room temperature are shown in Fig. 1(b). BFO and all La^{3+}-doped BFO compounds show similar XRD peaks, suggesting a rhombohedral structure. The stronger (100) and (200) peaks in La^{3+}-doped BFO suggest a preferred (100) crystallographic orientation. As indicated by the dashed line, the XRD peaks of BFO, BFO5L, BFO10L, and BFO15L do not shift, due to the close ion radii of La^{3+} (~1.16 Å) and Bi^{3+} (~1.17 Å).[46]

To identify the lanthanum doping effects on atomic vibrations, micro-Raman spectra were measured at room temperature as shown in Fig. 1(c), including Raman spectra of Bi_2O_3, Fe_2O_3, and La_2O_3 powders. The theoretical Raman active modes of the rhombohedral (*R*3*c* space group) $BiFeO_3$ can be summarized as the irreducible representation, $\Gamma = 4A_1 + 9E$.[47–49] The orthorhombic (*Pnma* space group) $LaFeO_3$ has Raman modes of $\Gamma = 7A_g + 5B_{1g} + 7B_{2g} + 5B_{3g}$.[49] As shown in Fig. 1(c), all compounds exhibit similar Raman vibrations, confirming the same *R*3*c* symmetry. As indicated by the dashed line, major Raman modes shift to higher frequencies because the La atom (atomic mass ~138.9 amu) is lighter than the Bi atom (~209 amu). Four dominant Raman vibrations are *E*(1) mode near 70 cm^{-1}, *E* (LO2) mode near 130 cm^{-1}, A_1(LO1) mode near 170 cm^{-1}, and A_1(LO2) mode near 220 cm^{-1}.[50]

Figure 2 shows fits of Raman modes in the region of 50–250 cm^{-1}. The *E*(1), *E*(2), and A_1(1) Raman modes in the La^{3+}-doped compounds exhibit slightly broadened spectra, which likely result from lattice anharmonicity and disorder produced by fluctuations in the A-site occupancies. The low-frequency Raman modes (below 170 cm^{-1}) and median frequency modes (150–270 cm^{-1}) are associated, respectively, with Bi and Fe atoms.[50] Raman modes above 260 cm^{-1} mainly correlate to oxygen motions. The vibration mode near 220 cm^{-1} is the A_1 tilt mode of the FeO_6 octahedra. The relative intensity of the *E*(2) mode grows as La concentration increases and the suppression of the A_1(1) mode is possibly due to the change in symmetry of the FeO_6 oxygen octahedra. The *E*(4) and *E*(8) modes near 280 and 480 cm^{-1} associate with atomic vibrations between A (or B)-site atoms and oxygen.[50] The prominent *E*(8) mode in BFO10L is possibly due to the enhancement of the La–O vibration.

The high-resolution TEM images and the selected area diffraction patterns (SADPs) were obtained for BFO, BFO5L, BFO10L, and BFO15L as shown in Fig. 3. The SADPs were measured from representative grains along the $[1\bar{1}0]$ zone axis. The $[1\bar{1}0]$ -viewed SADPs reveal 1/2(111) superlattice diffractions attributed to the tilted FeO_6 oxygen octahedra, indicating a rhombohedral *R*3*c* symmetry in $(Bi_{1-x}La_x)FeO_3$ (x = 0.0–0.15).[51,52] The TEM result confirms the rhombohedral phase as suggested in the XRD spectra [Fig. 1(b)]. Figure 3(c) reveals split diffraction spots (twinning) in BFO10L, suggesting the existence of twin planes corresponding to invariant plane shear as a variant boundary in martensite, which has been observed in ferroelectric materials and non-ferroic alloys.[53,54]

Figure 4 shows the high-resolution TEM domain structures in micrometer and nanometer scales. Compared with BFO10L, BFO5L and BFO15L show more homogeneous domain structures with domain wall widths of about 2–3 nm. Lamellar domains, such as 71° and 109° domains in rhombohedral structure, are often observed in crystal and ceramic grains, and serve to minimize the microstructural free energy.[54] The inset in Fig. 4(a) is a dark-field image viewed in a two-beam condition near the [110]-zone axis and imaged by a diffraction vector g = [111], which shows complicated domains. As indicated by the dashed circle in Fig 4(c), BFO10L exhibits complex pinning domain structures at the boundary intersections, which can cause high strain and decrease charge conductivity. Red and white arrows indicate 180° and non-180° domain walls, respectively. Enhanced electric conductivity has been reported along uniform domain walls in the (110)-oriented La^{3+}-doped BFO films.[55]

Figure 5(a) displays the Fe K-edge XANES spectra of $(Bi_{1-x}La_x)FeO_3$, and the referenced powders of FeO and Fe_2O_3. These absorption spectra reveal that the valence of Fe

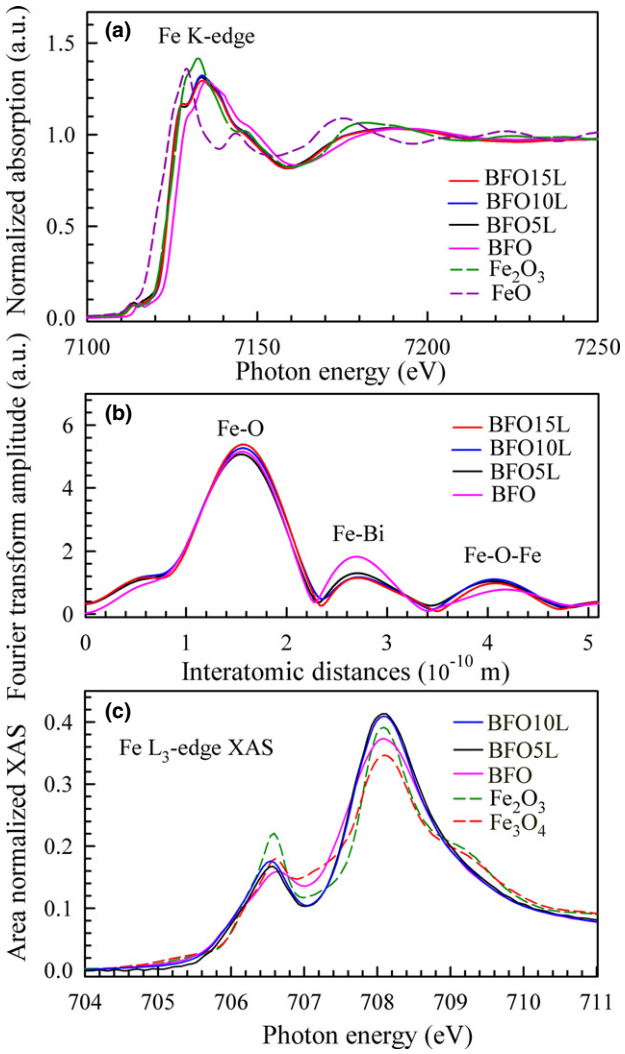


Fig. 5. (a) Fe K-edge XANES spectra vs. photon energy, (b) Fourier transform amplitude of $k^2\chi(k)$ versus interatomic distance without phase correction, and (c) Fe L_3-edge XAS of BFO, BFO5L, BFO10L and referenced materials.

ions in $(Bi_{1-x}La_x)FeO_3$ is +3 and the partial substitution of $Bi^{3+} \rightarrow La^{3+}$ does not cause valence change in $Fe^{3+} \rightarrow Fe^{4+}$. The Fourier transforms of the EXAFS $k^2\chi(k)$ spectra as shown in Fig. 5(b), indicate that the A-site La^{3+} doping does not obviously shift interatomic distances of Fe–O, Fe–Bi, and Fe–O–Fe bonds. These results suggest that the Fe–O–Fe bond angle is not modified by the La^{3+} substitution. Figure 5(c) shows the peak area normalized Fe L_3-edge XAS spectra and a shoulder feature develops at 706.4 eV with La doping. By comparing the evolution of the shoulder for Fe_2O_3 and Fe_3O_4, pure BFO and La^{3+}-doped BFO fit within the trend. The Fe energy is referenced to the Fe metal peak as determined by XAS + XPS.[56] The result is consistent with the Fe^{3+} valence as revealed in the Fe K-edge absorption.

The magnetization versus field plots at room temperature in Fig. 6 show no hysteresis loops. Instead, all compounds exhibit a similar linear antiferromagnetic behavior. The first-principles DFT for BFO suggests that oxygen vacancies (OVs) do not introduce magnetism, although a weak magnetization may develop in BFO under oxygen-rich condition.[27] The unchanged Fe^{3+} valence and Fe–O–Fe bond angle also suggest no enhancement of ferromagnetism as revealed in Fig. 5.

Figure 7 shows optical transmission spectra and $(\alpha h\nu)^2$ versus photon energy ($h\nu$). h and ν are Planck's constant and photon frequency. The optical absorption coefficient α is determined by the equation,

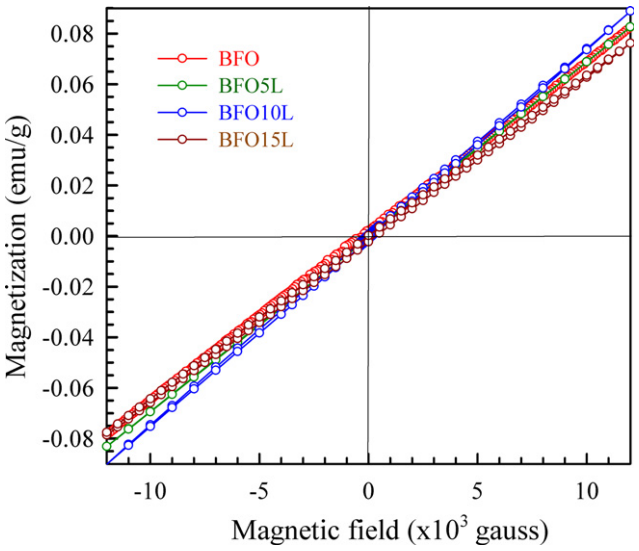


Fig. 6. Magnetization hysteresis loops at room temperature.

$$\alpha = -\ln(T)/d \quad (1)$$

where T and d are the measured optical transmission and sample thickness, respectively. The optical band gap can be estimated using the Tauc relation as follows,[45]

$$(\alpha h\nu)^2 = A(h\nu - E_g) \quad (2)$$

where E_g is the direct band gap between valence and conduction bands. E_g can be evaluated by extrapolating the straight lines of the curves of $(\alpha h\nu)^2$ vs $h\nu$ as shown in Fig. 7(b). The $(Bi_{1-x}La_x)FeO_3$ (x = 0.0–0.15) ceramics show slightly different optical absorption edges (E_g) in the range of 2.22–2.24 eV, which are smaller than band gaps of 2.60–2.68 eV for $(Bi_{1-x}La_x)FeO_3$ films (x = 0.0–0.30).[26] From first-principles DFT,[57,58] the presence of oxygen vacancies can shift the optical absorption edge to lower energy below the conduction band. An additional optical absorption peak appears at 2.2 eV for larger concentration of oxygen vacancies.[57] The band gap in BFO can be engineered from 2.09 to 2.32 eV by controlling particle sizes.[59] The decrease in band gap with decreasing particle size was attributed to the appearance of defect-induced levels between the conduction and valence bands, oxygen defects, and Coulombic interactions.[59] Thus, the variation in band gaps (2.22–2.24 eV) in $(Bi_{1-x}La_x)FeO_3$ is associated with oxygen vacancies and grain sizes.

Figure 8 shows open-circuit voltages (V_{oc}) and short-circuit current densities (J_{sc}) of ITO/$(Bi_{1-x}La_x)FeO_3$ ceramic/Au heterostructures as the laser was switched on and off with increasing intensity (I). The illuminated V_{oc} and J_{sc} are plotted in Fig. 9 as a function of illumination intensity. The ITO/$(Bi_{1-x}La_x)FeO_3$ ceramics/Au exhibit larger V_{oc} and J_{sc} than values obtained in the ITO/BFO ceramic/Au. For instance, at I ~910 W/m^2, V_{oc} and J_{sc} are 0.7 V and 0.09 A/m^2 in ITO/BFO ceramic/Au, 0.82 V and 2.07 A/m^2 in ITO/BFO5L/Au, 0.83 V and 0.58 A/m^2 in ITO/BFO10L/Au, and 0.78 V and 0.95 A/m^2 in ITO/BFO15L/Au. These PV values are larger than V_{oc} ~0.44 V and J_{sc}~0.25 A/m^2 reported in graphene/polycrystalline BFO/Pt films under standard white light (AM 1.5) of 1000 W/m^2.[36]

To understand the PV responses, a junction between n-type ITO film and p-type La^{3+}-doped BFO ceramic has been proposed to describe V_{oc} and J_{sc} as a function of illumination intensity.[38] We use Shockley's sign convention,[60] the diode current i_d under a bias voltage V is expressed as,[38]

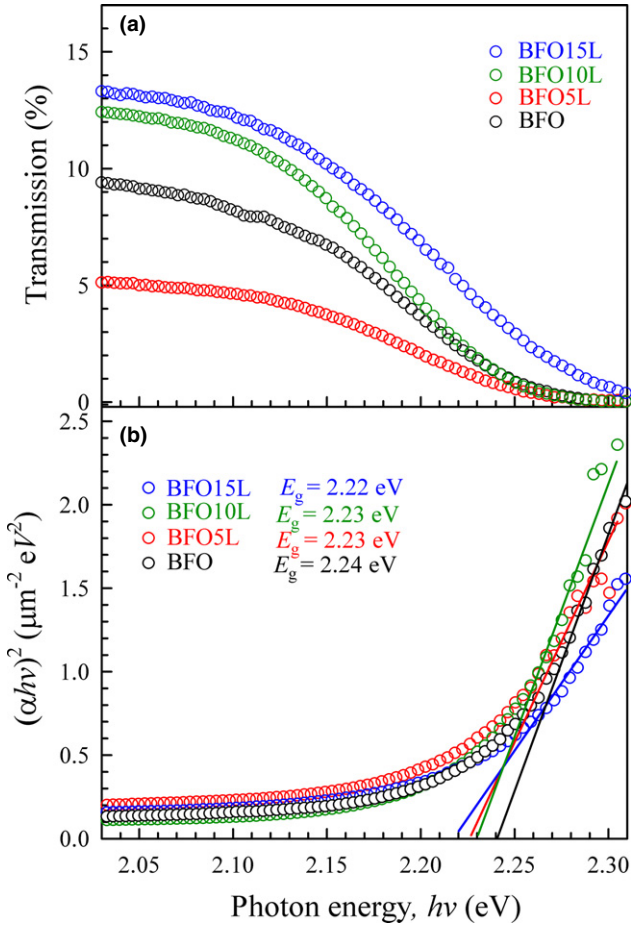


Fig. 7. (a) Optical transmission and (b) $(\alpha h\nu)^2$ versus photon energy.

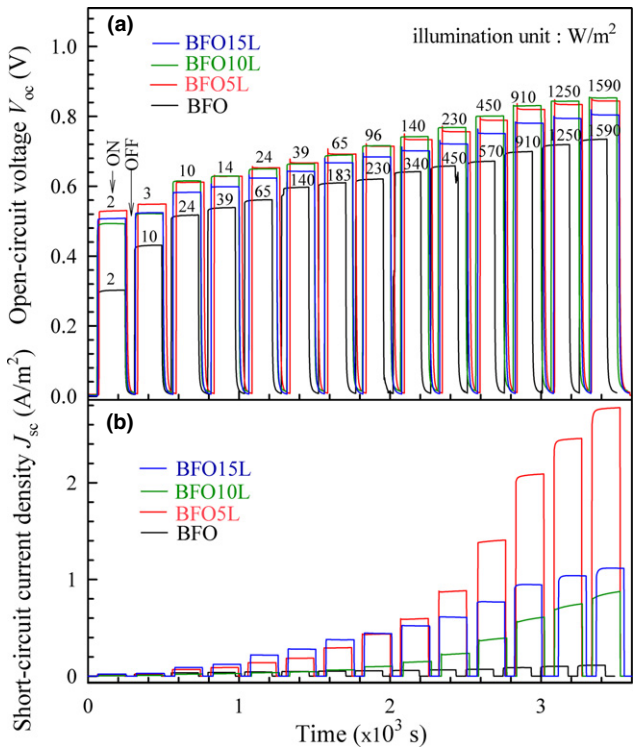


Fig. 8. (a) Open-circuit voltage (V_{oc}) and (b) short-circuit current density (J_{sc}) as light was switched on and off with increasing intensity. The labeled numbers are light intensities in W/m^2.

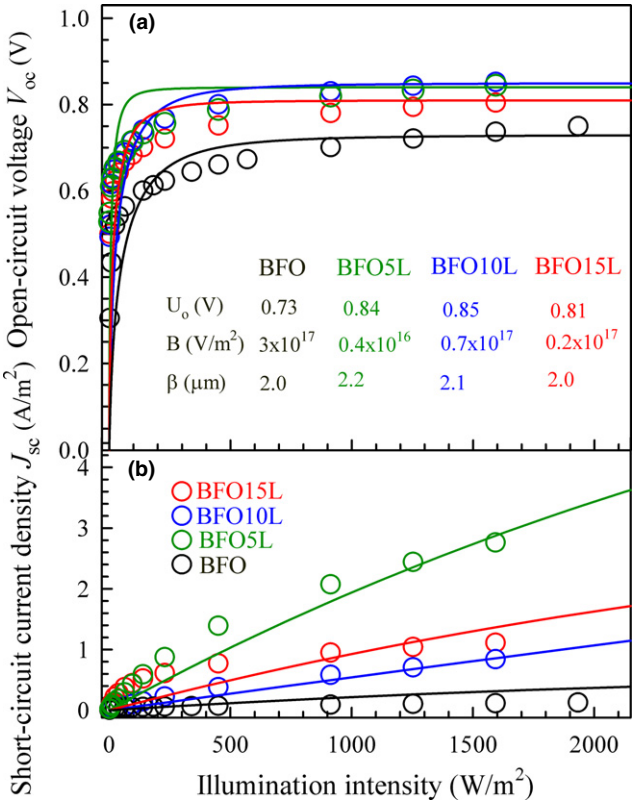


Fig. 9. (a) V_{oc} and (b) J_{sc} as a function of illumination intensity. The solid lines are the theoretical fits with parameters given in (a).

$$i_d = i_o\{\exp[q(V - i_d R_s)/\xi k_B T] - 1\} \quad (3)$$

where R_s and ξ are source resistance and diode quality factor. To estimate i_o, R_s, and ξ, the characteristic curves of current versus bias voltage were measured in the dark as shown in Fig. 10. By using Eq. (3) with $q = 1.6 \times 10^{-19}$ C, $k_B = 1.38 \times 10^{-23}$ J/K, and $T = 300$ K, we obtained $i_o = 5 \times 10^{-8}$ A, $R_s = 6.2 \times 10^4$ Ω, and $\xi = 13$ for BFO, $i_o = 5 \times 10^{-8}$ A, $R_s = 6.3 \times 10^3$ Ω, and $\xi = 13$ for BFO5L, $i_o = 5 \times 10^{-8}$ A, $R_s = 3.5 \times 10^3$ Ω, and $\xi = 13$ for BFO10L, and $i_o = 5 \times 10^{-8}$ A, $R_s = 1.26 \times 10^4$ Ω, and $\xi = 13$ for BFO15L. The quality factor ξ depends on grain size.[38,61] From Eq. (3), the measured current i can be expressed as a function of measured voltage under illumination by,[38]

$$i = i_p - i_d = i_p - i_o(\exp\{[V - (i_d - i_p)R_s]q/\xi kT\} - 1) \quad (4)$$

where i_p and i_d are photovoltaic and diode currents. Through considerable derivations,[38] short-circuit current (i_{sc}) and open-circuit voltage (V_{oc}) can be expressed as,[38]

$$i_{sc} = (U_o/R_s) - B\beta^2\{i_{sc} + i_o[\exp(i_{sc}R_s q/\xi kT) - 1]\}^2/(R_s i_I^2) \quad (5)$$

$$V_{oc} = U_o - B\beta^2 i_o^2[\exp(V_{oc}q/\xi kT) - 1]^2/i_I^2 \quad (6)$$

$$iI = q\lambda I/hc; B = (qn_p/2\varepsilon_o\varepsilon_p)(1 + n_p\varepsilon_p/\varepsilon_n n_n) \quad (7)$$

where S, λ, and c are illumination area, wavelength, and light speed. U_o is the voltage step across the depletion region at dark and β is the attenuation length. From Fig. 7, the measured attenuation lengths ($\beta = 1/\alpha$) at $\lambda = 405$ nm are, respectively, about 2.0, 2.2, 2.1, and 2.0 μm for BFO,

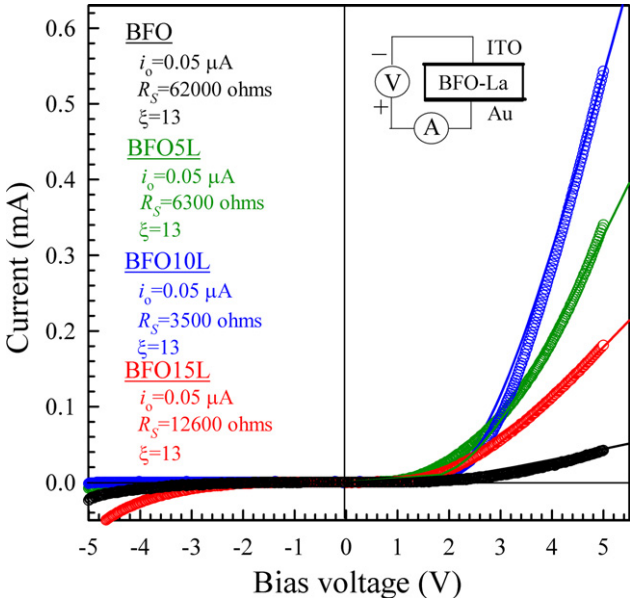


Fig. 10. Characteristic curves of current versus bias voltage without illumination.

BFO5L, BFO10L, and BFO15L. n_p and n_n are carrier densities of p-type La-doped BFO ceramics and n-type ITO film. ε_p and ε_n are, respectively, dielectric permittivities of p-type-doped BFO ceramics and n-type ITO film. The ε_p values of BFO, BFO5L, BFO10L, and BFO15L ceramics are, respectively, about 100, 200, 160, and 155 for frequency f = 1 MHz at room temperature. The solid lines in Fig. 9 are theoretical fits of V_{oc} and J_{sc} ($=i_{sc}/S$) by using Eqs. (5) and (6) with fitting parameters given in Fig. 9(a). The fits of V_{oc} agree reasonably well with experimental results. The fits of J_{sc} show slight discrepancy with the experimental values in the low illumination region possibly due to current leakage. The estimated carrier densities (n_p ~$2B\varepsilon_o\varepsilon_p/q$) of BFO, BFO5L, BFO10L, and BFO15L ceramics are, respectively, 5.1 × 10^{25}, 0.6 × 10^{25}, 2.7 × 10^{25}, and 1.7 × 10^{25} m^{-3}. The unilluminated depletion region widths $[d_o\sim(U_o/B)^{1/2}]$[38] of BFO, BFO5L, BFO10L, and BFO15L are, respectively, about 1.6, 14.5, 3.5, and 5.2 nm, which are smaller than the depletion layer (few hundred nanometers) between ITO and BFO films.[32] Note that this junction-like model only considers the photo-excited electron-hole creation. Other factors, such as current leakage, oxygen vacancies, internal reflection, domain structure, and charge recombination can also influence PV conductivity.[62]

Figure 11 shows curves of power conversion efficiency (η) versus load voltage (V) for several intensities. The maximal PV power conversion efficiencies η_{max} of ITO/BFO/Au, ITO/BFO5L/Au, ITO/BFO10L/Au, and ITO/BFO15L/Au at I~2 W/m^2 can, respectively, reach 0.014%, 0.17%, 0.031%, and 0.19%, which are larger than η_{max} ~0.0025% in graphene/polycrystalline BFO/Pt films (under white light of I ~10^3 W/m^2),[36] η_{max} ~0.005% in Au/polycrystalline BFO/Pt,[35] and η_{max} ~0.007% in ITO/$(Bi_{0.90}Ca_{0.10})FeO_{2.95}$/Au (under illumination of λ = 405 nm).[38]

IV. Summary

High-resolution TEM, XRD, and micro-Raman spectra reveal a rhombohedral $R3c$ symmetry in $(Bi_{1-x}La_x)FeO_3$ (x = 0.0–0.15). The low-frequency Raman modes become broader and shift toward higher frequency as La^{3+} increases. The Fe K-edge synchrotron absorption confirms that Fe^{3+} valence and Fe–O–Fe bond angle are not modified by the La^{3+} substitution. The maximal power conversion efficiency

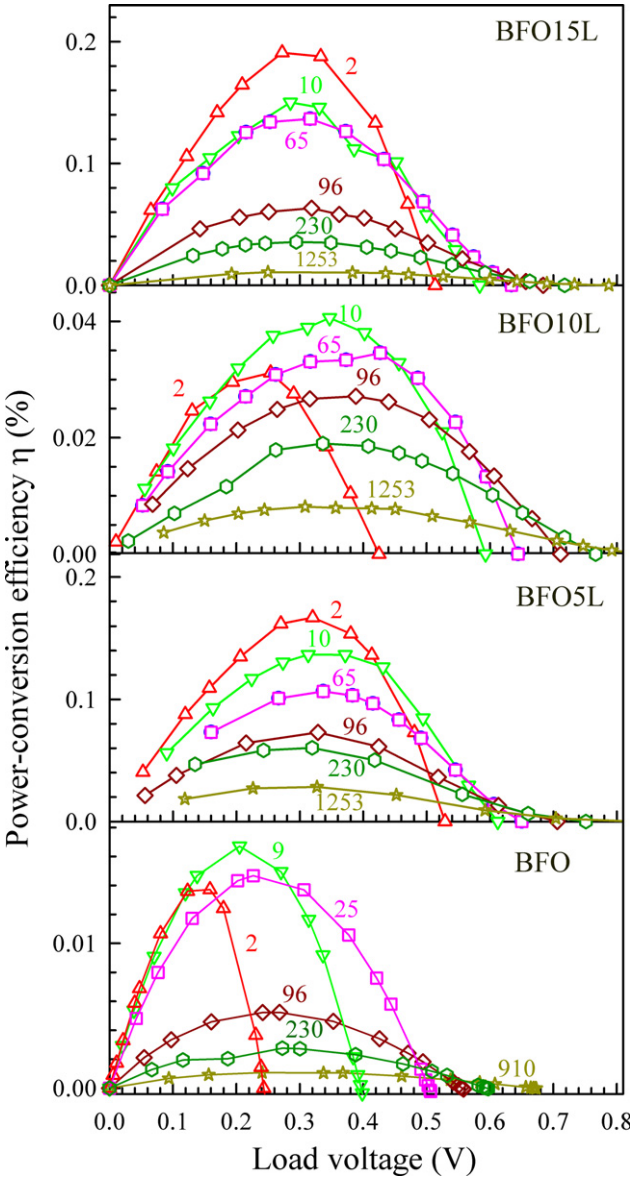


Fig. 11. Power conversion efficiency (η) versus load voltage. The labeled numbers are illumination intensities in W/m^2.

of ITO/BFO15L/Au can reach 0.19%. The homogeneous domain structure plays an important role in the enhanced PV responses of BFO5L and BFO15L. A p–n junction-like model based on optically excited charges in the depletion region between ITO and $(Bi_{1-x}La_x)FeO_3$ can reasonably describe V_{oc} and J_{sc} as a function of illumination intensity. The smaller band gaps (2.22–2.24 eV) in $(Bi_{1-x}La_x)FeO_3$ (x = 0.0–0.15) ceramics can be correlated with oxygen vacancies and grain sizes.

Acknowledgment

This project is supported by the Ministry of Science and Technology of Taiwan under Project Nos. 103-2112-M-030-001, 103-2221-E-146-001, and 102-2221-E-131-006. The Advanced Light Source (ALS) is supported by the Director, Office of Science, Office of Basic Energy Sciences, of the U.S. Department of Energy under contract no. DE-AC02-05CH11231.

References

[1]G. Catalan and J. F. Scott, "Physics and Applications of Bismuth Ferrite," *Adv. Mater.*, **21**, 2463–85 (2009).

[2]A. M. Glazer, "Classification of Tilted Octahedral in Perovskites," *Acta Crystallogr. B*, **28**, 3384–92 (1972).

[3]P. Ravindran, R. Vidya, A. Kjekshus, H. Fjellvåg, and O. Eriksson, "Theoretical Investigation of Magnetoelectric Behavior in $BiFeO_3$," *Phys. Rev. B*, **74**, 224412, 18pp (2006).
[4]I. Sosnowska, T. Peterlin-Neumaier, and E. Steichele, "Spiral Magnetic Ordering in Bismuth Ferrite," *J. Phys. C*, **15**, 4835–46 (1982).
[5]T. Rojac, H. Ursic, A. Bencan, B. Malic, and D. Damjanovic, "Mobile Domain Walls as a Bridge Between Nanoscale Conductivity and Macroscopic Electromechanical Response," *Adv. Funct. Mater.*, **25**, 2099–108 (2015).
[6]D. C. Arnold, "Composition-Driven Structural Phase Transitions in Rare-Earth-Doped $BiFeO_3$ Ceramics: A Review," *IEEE Trans. Ultrason. Ferroelectr. Freq. Control*, **61**, 62–82 (2015).
[7]T. T. Carvalho, et al., "Room Temperature Structure and Multiferroic Properties in $Bi_{0.7}La_{0.3}FeO_3$ Ceramics," *J. Alloy. Compd.*, **554**, 97–103 (2013).
[8]X. Yan, J. Chen, Y. Qi, J. Cheng, and Z. Meng, "Hydrothermal Synthesis and Characterization of Multiferroic $Bi_{1-x}La_xFeO_3$ Crystallites," *J. Eur. Ceram. Soc.*, **30**, 265–9 (2010).
[9]J. H. Lee, et al., "Variations of Ferroelectric off-Centering Distortion and *sd*-4*p* Orbital Mixing in La-Doped $BiFeO_3$ Multiferroics," *Phys. Rev. B*, **82**, 045113, 8pp (2010).
[10]D. S. Garcia-Zaleta, A. M. Torres-Huerta, M. A. Dominguez-Crespo, J. A. Matutes-Aquino, A. M. Gonzalez, and M. E. Villafuerte-Castrejon, "Solid Solutions of La-Doped $BiFeO_3$ Obtained by the Pechini Method with Improvement in Their Properties," *Ceram. Int.*, **40**, 9225–33 (2014).
[11]D. A. Rusakov, A. M. Abakumov, K. Yamaura, A. A. Belik, G. V. Tendeloo, and E. Takayama-Muromachi, "Structural Evolution of the $BiFeO_3$-$LaFeO_3$ System," *Chem. Mater.*, **23**, 285–92 (2011).
[12]V. James, P. P. Rao, S. Sameera, and S. Divya, "Multiferroic Based Reddish Brown Pigments: $Bi_{1-x}M_xFeO_3$ (M= Y and La) for Coloring Applications," *Ceram. Int.*, **40**, 2229–35 (2014).
[13]K. Sen, K. Singh, A. Gautum, and M. Singh, "Dispersion Studies of La Substitution on Dielectric and Ferroelectric Properties of Multiferroic $BiFeO_3$ Ceramics," *Ceram. Int.*, **38**, 243–9 (2012).
[14]Y. Du, X. Cheng, M. Shahbazi, E. W. Collings, S. X. Dou, and X. L. Wang, "Enhancement of Ferromagnetic and Dielectric Properties in Lanthanum Doped $BiFeO_3$ by Hydrothermal Synthesis," *J. Alloys Compd*, **490**, 637–41 (2010).
[15]Z. Chen, J. Hu, Z. Lu, and X. He, "Low-Temperature Preparation of Lanthanum-Doped $BiFeO_3$ Crystallites by a Sol–Gel Hydrothermal Method," *Ceram. Int.*, **37**, 2359–64 (2011).
[16]V. Antonov, I. Georgieva, N. Trendafilova, D. Kovacheva, and K. Krezhov, "First Principles Study of Structure and Properties of La and Mn-Modified $BiFeO_3$," *Solid State Ion*, **14**, 782–8 (2012).
[17]J. H. Lee, M. A. Oak, H. J. Choi, J. Y. Son, and H. M. Jang, "Rhombohedral-Orthorhombic Morphotropic Phase Boundary in $BiFeO_3$-Based Multiferroics: First Principles Prediction," *J. Mater. Chem.*, **22**, 1667–72 (2012).
[18]O. E. Gonzalez-Vazquez, J. C. Wojdel, O. Dieguez, and J. Iniguez, "First Principles Investigation of the Structural Phases and Enhanced Response Properties of the $BiFeO_3$-$LaFeO_3$ Multiferroic Solid Solutions," *Phys. Rev. B*, **85**, 064119, 10pp (2012).
[19]S.-T. Zhang, et al., "Substitution-Induced Phase Transition and Enhanced Multiferroic Properties of $Bi_{1-x}La_xFeO_3$ Ceramics," *Appl. Phys. Lett.*, **88**, 162901, 3pp (2006).
[20]Q. H. Jiang and C. W. Nan, "Synthesis and Properties of Multiferroic La-Modified $BiFeO_3$ Ceramics," *J. Am. Ceram. Soc.*, **89**, 2123–7 (2006).
[21]G. L. Bras, P. Bonville, D. Colson, A. Forget, N. Genand-Riondet, and R. Tourbot, "Effect of La Doping in the Multiferroic Compound $BiFeO_3$," *Phys. B*, **406**, 1492–5 (2011).
[22]Y. H. Lin, Q. Jiang, Y. Wang, C. W. Nan, L. Chen, and J. Yu, "Enhancement of Ferromagnetic Properties in $BiFeO_3$ Polycrystalline Ceramic by La Doping," *Appl. Phys. Lett.*, **90**, 172507, 3pp (2007).
[23]G. L. Yuan, S. W. Or, J. M. Liu, and Z. G. Liu, "Structural Transformation and Ferroelectromagnetic Behavior in Single-Phase $Bi_{1-x}Nd_xFeO_3$ Multiferroic Ceramics," *Appl. Phys. Lett.*, **89**, 052905, 3pp (2006).
[24]G. L. Yuan and S. W. Or, "Multiferroicity in Polarized Single-Phase $Bi_{0.875}Sm_{0.125}FeO_3$ Ceramics," *J. Appl. Phys.*, **100**, 024109, 5pp (2006).
[25]P. Pandit, S. Satapathy, P. Sharma, P. K. Gupta, S. M. Yusuf, and V. G. Sathe, "Structural, Dielectric and Multiferroic Properties of Er and La Substituted $BiFeO_3$ Ceramics," *Bull. Mater. Sci.*, **34**, 899–905 (2011).
[26]N. Kumar, A. Kaushal, C. Bhardwaj, and D. Kaur, "Effect of La Doping on Structural, Optical and Magnetic Properties of $BiFeO_3$ Thin Films Deposited by Pulsed Laser Deposition Technique," *Optoelectr. Adv. Mater.*, **4**, 1497–502 (2010).
[27]J. Hemberger, P. Lunkenheimer, R. Fichtl, H. A. Krug von Nidda, V. Tsurkan, and A. Loidl, "Relaxor Ferroelectricity and Colossal Magnetocapacitive Coupling in Ferromagnetic $CdCr_2S_4$," *Nature*, **434**, 364–7 (2005).
[28]I. Levin, et al., "Displacive Phase Transition and Magnetic Structures in Nd-Substituted $BiFeO_3$," *Chem. Mater.*, **23**, 2166–75 (2011).
[29]M. Khodabakhsh, C. Sen, H. Kassaf, M. A. Gulun, and I. B. Misirlioglu, "Strong Smearing and Disappearance of Phase Transitions into Polar Phases Due to Inhomogeneous Lattice Strains Induced by A-Site Doping in $Bi_{(1-x)}A_{(x)}FeO_3$ (A: La, Sm, Gd)," *J. Alloys Compd*, **604**, 117–29 (2014).
[30]Q. Xu, M. Sobhan, Q. Yang, F. Anariba, K. P. Ong, and P. Wu, "The Role of Bi Vacancies in the Electrical Conduction of $BiFeO_3$: A First-Principles Approach," *Dalton Trans.*, **43**, 10787–93 (2014).
[31]T. R. Paudel, S. S. Jaswal, and E. Y. Tsymbal, "Intrinsic Defects in Multiferroic $BiFeO_3$ and Their Effect on Magnetism," *Phys. Rev. B*, **85**, 104409, 8pp (2012).
[32]S. Y. Yang, et al., "Photovoltaic Effects in $BiFeO_3$," *Appl. Phys. Lett.*, **95**, 062909, 3pp (2009).
[33]H. Kim, et al., "Electrical, Optical, and Structural Properties of Indium-Tin-Oxide Thin Films for Organic Light-Emitting Devices," *J. Appl. Phys.*, **86**, 6451–61 (1999).
[34]T. Choi, S. Lee, Y. J. Choi, V. Kiryukhin, and S. W. Cheong, "Switchable Ferroelectric Diode and Photovoltaic Effect in $BiFeO_3$," *Science*, **324**, 63–6 (2009).
[35]B. Chen, et al., "Effect of Top Electrodes on Photovoltaic Properties of Polycrystalline $BiFeO_3$ Based Thin Film Capacitors," *Nanotechnology*, **22**, 195201, 5pp (2011).
[36]Y. Zang, et al., "Enhanced Photovoltaic Properties in Graphene/Polycrystalline $BiFeO_3$/Pt Heterojunction Structure," *Appl. Phys. Lett.*, **99**, 132904, 3pp (2011).
[37]B. Kundys, M. Viret, D. Colson, and D. O. Kundys, "Light-Induced Size Changes in $BiFeO_3$ Crystals," *Nat. Mater.*, **9**, 803–5 (2010).
[38]C. S. Tu, et al., "Calcium-Doping Effects on Photovoltaic Response and Structure in Multiferroic $BiFeO_3$ Ceramics," *J. Appl. Phys.*, **114**, 124105, 6pp (2013).
[39]C. S. Tu, C.-M. Hung, V. H. Schmidt, R. R. Chien, M. D. Jiang, and J. Anthoninappen, "The Origin of Photovoltaic Responses in $BiFeO_3$ Multiferroic Ceramics," *J. Phys.: Condensed Matter*, **24**, 495902, 5pp (2012).
[40]C. S. Tu, Z. R. Xu, V. H. Schmidt, T. S. Chan, R. R. Chien, and H. Son, "A-Site Strontium Doping Effects on Structure, Magnetic, and Photovoltaic Properties of $(Bi_{1-x}Sr_x)FeO_3$ Multiferroic Ceramics," *Ceram. Int.*, **41**, 8417–24 (2015).
[41]D. Rout, K. S. Moon, and S. J. L. Kang, "Temperature-Dependent Raman Scattering Studies of Polycrystalline $BiFeO_3$ Bulk Ceramics," *J. Raman Spectrosc.*, **40**, 618–26 (2009).
[42]S. R. Basu, et al., "Photoconductivity in $BiFeO_3$ Thin Films," *Appl. Phys. Lett.*, **92**, 091905, 3pp (2008).
[43]X. S. Xu, et al., "Optical Properties and Magnetochromism in Multiferroic $BiFeO_3$," *Phys. Rev. B*, **79**, 134425, 4pp (2009).
[44]X. Chen, H. Zhang, T. Wang, F. Wang, and W. Shi, "Optical and Photoluminescence Properties of $BiFeO_3$ Thin Films Grown on ITO-Coated Glass Substrates by Chemical Solution Deposition," *Phys. Status Solidi A*, **209**, 1456–60 (2012).
[45]Y. Xu and M. Shen, "Structure and Optical Properties of Nanocrystalline $BiFeO_3$ Films Prepared by Chemical Solution Deposition," *Mater. Lett.*, **62**, 3600–2 (2008).
[46]R. D. Shannon, "Revised Effective Ionic Radii and Systematic Studies of Interatomic Distances in Halides and Chalcogenides," *Acta Cryst A*, **32**, 751–67 (1976).
[47]P. Hermet, M. Gofinet, J. Kreisel, and Ph. Ghosez, "Raman and Infrared Spectra of Multiferroic Bismuth Ferrite from First Principles," *Phys. Rev. B*, **75**, 220102(R), 4pp (2007).
[48]J. Hlinka, J. Pokorny, S. Karimi, and I. M. Reaney, "Angular Dispersion of Oblique Phonon Modes in $BiFeO_3$ from Micro-Raman Scattering," *Phys. Rev. B*, **83**, 020101(R), 4pp (2011).
[49]J. Bielecki, et al., "Structural and Magnetic Properties of Isovalently Substituted Multiferroic $BiFeO_3$: Insights from Raman Spectroscopy," *Phys. Rev. B*, **86**, 184422, 16pp (2012).
[50]K. Sinha, A. Mascarenhas, G. S. Horner, K. A. Bertness, S. R. Kurtz, and J. M. Olson, "Raman Line-Shape Analysis of Random and Spontaneously Ordered $GaInP_2$ Alloy," *Phys. Rev. B*, **50**, 7509–13 (1994).
[51]D. I. Woodward and I. M. Reaney, "Electron Diffraction of Tilted Perovskites," *Acta Crystallogr. B*, **61**, 387–99 (2005).
[52]C. W. Tai, S. H. Choy, and H. L. W. Chan, "Ferroelectric Domain Morphology Evolution and Octahedral Tilting in Lead-Free $(Bi_{1/2}Na_{1/2})TiO_3$-$(Bi_{1/2}K_{1/2})TiO_3$-$(Bi_{1/2}Li_{1/2})TiO_3$- $BaTiO_3$ Ceramics at Different Temperatures," *J. Am. Ceram. Soc.*, **91**, 3335–41 (2008).
[53]B. M. Park and S. J. Chung, "Optical, Electron Microscopic, and X-ray Topographic Studies of Ferroic Domains in Barium Titanate Crystals Grown from High-Temperature Solution," *J. Am. Ceram. Soc.*, **77**, 3193–201 (1994).
[54]C. C. Chou and C. S. Chen, "Banded Domain Structures and Polarization Arrangements in $PbTiO_3$ Single Crystals," *Ceram. Int.*, **26**, 693–7 (2000).
[55]J. Seidel, et al., "Domain Wall Conductivity in La-Doped $BiFeO_3$," *Phys. Rev. Lett.*, **105**, 197603, 3pp (2010).
[56]C. T. Chen, et al., "Experimental Confirmation of the X-ray Magnetic Circular Dichroism sum Rules for Iron and Cobalt," *Phys. Rev. Lett.*, **75**, 152–5 (1995).
[57]S. Ju and T. Y. Cai, "First-Principles Studies of the Effect of Oxygen Vacancies on the Electronic Structure and Linear Optical Response of Multiferroic $BiFeO_3$," *Appl. Phys. Lett.*, **95**, 231906, 3pp (2009).
[58]S. J. Clark and J. Robertson, "Energy Levels of Oxygen Vacancies in $BiFeO_3$ by Screened Exchange," *Appl. Phys. Lett.*, **94**, 022902, 3pp (2009).
[59]P. S. V. Mocherla, C. Karthik, R. Ubic, M. S. Ramachandra, and C. Sudakar, "Tunable Bandgap in $BiFeO_3$ Nanoparticles: The Role of Microstrain and Oxygen Defects," *Appl. Phys. Lett.*, **103**, 022910, 5pp (2013).
[60]W. Shockley and H. J. Queisser, "Detailed Balance Limit of Efficiency of *p–n* Junction Solar Cells," *J. Appl. Phys.*, **32**, 510–9 (1961).
[61]K. Sen and B. P. Tyagi, "Diode Quality Factor in Polycrystalline Solar Cells," *J. Appl. Phys.*, **56**, 1240–1 (1984).
[62]N. A. Spaldin, S.-W. Cheong and R. Ramesh, "Multiferroics: Past, Present, and Future," *Phys. Today*, **63**, 38–43 (2010). □